Indian Journal of Pure & Applied Physics
Vol. 62, September 2024, pp. 813-824
DOI: 10.56042/ijpap.v62i9.9809

Buoyancy-driven unsteady Flow of Casson-Williamson Fluid through a Vertical Stretching Sheet with Cross-diffusion Effect

Kiran Kunwar Chouhan & Santosh Chaudhary*

Department of Mathematics, Malaviya National Institute of Technology, Jaipur 302 017, India

Received 22 March 2024; accepted 1 August 2024

This article proclaims Casson-Williamson fluid's buoyancy assisting and opposing flow through a vertical stretching sheet. The flow is intended to be two-dimensional, unsteady, and laminar by examining the viscous dissipation, Joule heating, and cross-diffusion effects. Further, this study is performed under thermal radiation, Brownian motion, and thermophoresis effects. The mathematical model is developed by considering the combined characteristics of the Casson and Williamson fluid model. Developed mathematical model is simplified using competent similarity variables, and the acquired system of an ordinary differential equation is operated with BVP Midrich method. Finally, graphical results are produced for momentum, thermal, and mass profile in both buoyancy assisting and buoyancy opposing flow cases. Impact of all emerging variables on local skin friction coefficient, Nusselt, and Sherwood numbers is illustrated through numerical data in table format.

Keywords: Buoyancy force; Casson-williamson fluid; Cross-diffusion effect; Brownian motion; Thermophoresis

1 Introduction

Buoyancy effects become significant when there is a considerable difference between particles and fluid densities. These effects are accountable for sediment formation or flotation of the fluid particles. Buoyancy-driven flows close to a heated wall have immense engineering uses. For instance, ventilation construction, nuclear reactor confinement, and geophysical flows[1,2]. Makinde *et al.*[3] examined the buoyancy-driven MHD flow of nanofluids through a stretching or shrinking sheet along a convective boundary condition. They observed that the Sherwood number reduces with an increasing buoyancy ratio. Ahmad *et al.*[4] discussed how buoyancy forces impact nanofluid flow through a vertical Riga plate along convective heat transfer. Lund *et al.*[5] performed a numerical analysis on a dual solution of buoyancy-driven micropolar nanofluid flow with magnetic field effect over a vertical stretching surface. Iqbal *et al.*[6] examined the buoyancy impact on unsteady magnetohydrodynamic flow of Maxwell fluid through a vertical stretching sheet and observed that fluid velocity enhances with thermal buoyancy parameter.

Fluids that contravene Newton's law of viscosity are labeled as non-Newtonian fluids. Some examples of non-Newtonian fluids are printing ink, sugar solution, clay coatings, silly putty, and certain oils. Researchers have emphasized this genre of fluids due to its high demand and relevance in diverse industry sectors such as the mining industry, food processing industries, chemical and plastic processing industries, in processes such as petroleum product extraction from crude oil, bioengineering processing, heat transmission processes, and refrigeration systems, etc. Non-Newtonian fluids possess supremely complex mathematical expressions as compared to Newtonian fluids. Numerous fluid models to characterize diverse non-Newtonian fluid models are referred to as Jeffrey, Burger, Oldroyd-B, Casson, Walter's B, Maxwell, Carreau, Seely, Sisko, Bulky, and Eyring-Powell fluids. Casson fluid is identified for its dilatation and shear thinning features, which can behave as a solid as well as a fluid based on various circumstances. Some examples of Casson nanofluids are human blood, mayonnaise, honey, tomato ketchup, soup, and jelly. The Williamson fluid also holds the shear-thinning property. Khan *et al.*[7] examined the Williamson fluid flow with a chemically reactive species. Nadeem and Hussain[8] analyzed the boundary layer flow of Williamson nanofluid flow through a stretching sheet. Khan and Khan[9] discussed Blasius, Sakiadis, Stretching, and Stagnation-Point flow conditions over Williamson fluid flow. There are non-

*Corresponding author:
(E-mail: d11.santosh@yahoo.com, kiranchouhanudr@gmail.com)

Newtonian fluids possess integrated physical characteristics of Casson and Williamson fluids, which can be termed the Casson-Williamson model. Humane *et al*.[10] considered Casson-Williamson fluid flow through a porous stretching sheet. Kumaran *et al*.[11] numerically scrutinized cross-diffusion effect on MHD flow of Casson-Maxwell fluid through an elastic sheet. Later on, many researchers considered Casson-Williamson fluid flow subjected to various conditions, such as, Akolade and Tijani[12], Ogunseye *et al*.[13], Humane *et al*.[14], and Jangid *et al*.[15].

When the heat and mass conveyance phenomena materialize simultaneously between the fluxes, as in chemical engineering or geotechnical systems, there occurs a cross-diffusion phenomena, entitled as Soret and Dufour effects. In particular, Soret effect or thermal-diffusion is a procedure in which mass transfer occurs in a medium due to temperature difference, whereas Dufour or diffusion-thermo effect is characterized as the transfer of heat under the action of concentration gradient. Generally, such repercussions are disregarded in the heat and mass transfer processes as both hold absolute magnitude of lower order as compared to effects depicted in Fourier's or Fick's law. However, these effects cannot be abandoned in operations engaging with higher temperature or concentration gradient, like, chemical fabrication, isotope segregation, insulation of materials, disposal of nuclear waste and fusion of gases having low molecular mass, oil reservoirs and several other industrial and engineering processes. Hayat *et al*.[16] discussed Soret and Dufour effects on magnetohydrodynamic boundary layer flow of Casson fluid. Kumaran and Sandeep[17] investigated Brownian movement and thermophoresis impact on parabolic flow of Casson-Williamson fluid by giving consideration to Soret-Dufour phenomena. Mabood *et al*.[18] formed a mathematical model to illustrate Soret or Dufour effects, entropy generation and irreversibility process in Casson fluid flow through a stretching sheet with a non-linear stretching rate. Recently, Ramudu *et al*.[19] executed a numerical investigation concerning Soret/Dufour effects on Casson fluid flow under magnetic field and convective diffusion phenomena.

The motion of fluid particles exceedingly impacts the attributes of fluid flows. The haphazard and erratic movement of the suspended particles caused by their continuous collision with other rapidly moving particles in any fluid is introduced as Brownian motion. The thermophoresis effect emerges due to the temperature gradient in a suspended composite of particles and fluids. In this phenomenon, fluid particles migrate in bulk from the hot zone to lower-temperature regions. Buongiorno[20] considered seven different slip procedures and deduced that thermophoresis and Brownian motion are the only essential slip procedure in nanofluids. Anbuchezhian *et al*.[21] investigated Brownian motion and thermophoresis effects on nanofluid flow through a vertical stretching surface subjected to varying stream conditions. A numerical investigation on non-Newtonian third-grade fluid flow through a pressure-type die under the impact of Brownian diffusion and thermophoresis was carried out by Mahanthesh and Joseph[22]. Mittal and Patel[23] discussed Brownian motion and thermophoresis impact on the MHD flow of Casson nanofluid along mixed convection, thermal radiation, and heat generation. Recently, Sulochana and Mahalaxmi[24] considered thermophoretic diffusion and Brownian motion influence Williamson fluid flow over an elastic sheet along radiation and chemical reaction. Chaudhary and Chouhan[25] carried out a numerical study concerning Brownian motion and thermophoresis influence on Darcy-Forchheimer flow of Prandl-Eyring fluid through a Riga plate of variable thickness.

Despite the extensive research conducted by numerous scholars on the impact of buoyancy forces and cross-diffusion effects in various non-Newtonian fluid models, there remains a significant gap in the literature when it comes to investigating the buoyancy-assisting and opposing flows of Casson-Williamson fluids in the context of vertical stretching sheets, while taking into account the effects of viscous fluid dissipation, Joule heating, and cross-diffusion. Thus, the primary aim of this article is to fill this research gap by addressing the aforementioned problem. In addition to these factors, the study also considers the influence of thermal radiation, Brownian motion, and thermophoresis, providing a comprehensive examination of their combined effects on the flow dynamics and transport properties of the Casson-Williamson fluid in this particular configuration. The mathematical model's leading equations are operated with pertinent similarity transformations and reformed to a collection of ordinary differential equations. Later, which are computationally determined through the BVP Midrich scheme, and outcomes are elucidated figuratively

pertaining to dimensionless velocity, temperature, and concentration profiles. This study has the potential to yield substantial real-world benefits across a range of industries, for instance, thin film coating in materials processing, cooling and heat exchangers in electronics, materials manufacturing in space, magnetic hyperthermia for cancer treatment, oil and gas reservoir engineering, bioprocess engineering, and geophysical fluid dynamics.

2 Mathematical Framework

In the current study, a time-dependent, two-dimensional, incompressible flow of Casson-Williamson fluid is intended to scrutinize the cross-diffusion, Brownian diffusion, and thermophoresis processes. The flow is considered over a vertical stretching sheet (Fig. 1) under buoyancy force effects on assisting and opposing regions. The transverse consistent magnetic field force with the intensity B_0 is exerted in the flow domain. Therefore, the Joule heating, linear thermal radiation, and viscous dissipation effect are integrated to analyze the thermal characteristics of the flow field. The vertical surface is placed at the coordinate axis $y=0$ with stretching velocity $U_s=\frac{cx}{1-\delta t}$ in the vertical direction. The non-Newtonian fluid surrounds along the region $y>0$. The expression for free stream velocity, temperature, and concentration is stated as follows

$$U_\infty=\frac{ax}{1-\delta t},\qquad T_\infty=T_s-\frac{bx}{1-\delta t},$$

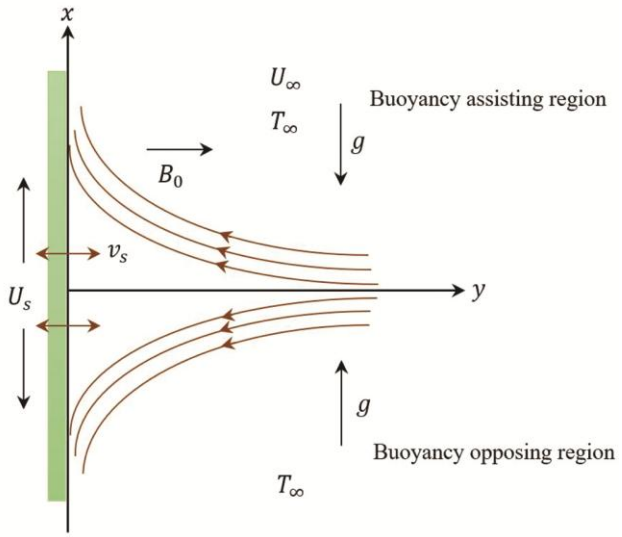

Fig. 1 — Physical conformation of the flow problem

$$C_\infty=C_s-\frac{bx}{1-\delta t} \qquad \ldots(1)$$

In the above equations, subscript s refers the surface, c stands for stretching coefficient, $\delta>0$ is the unsteadiness parameter, t refers the time, T stands for the temperature, C symbolize concentration, U_∞, T_∞ and C_∞ represent the atmosphere velocity, temperature and concentration, respectively, $a>0$ and $b>0$ are parameters representing strength of stagnation flow.

The rheological model of an isotropic and incompressible Casson fluid flow is stated below[26]

$$\tau'_{ij}=\begin{cases}2\left(\mu_\varepsilon+\dfrac{P_y}{\sqrt{2\pi}}\right)e_{ij} & when \quad \pi>\pi_c\\ 2\left(\mu_\varepsilon+\dfrac{P_y}{\sqrt{2\pi}}\right)e_{ij} & when \quad \pi<\pi_c\end{cases} \qquad \ldots(2)$$

where, τ'_{ij} is the $(i,j)^{th}$ constituent of Cauchy stress tensor, μ_ε stands for coefficient of viscosity of plastic non-Newtonian fluid $(\mu_\varepsilon=\rho\nu)$, P_y denotes the produced stress of the fluid, π refers the product of the constituents of distortion estimate with itself, π_c is the critical value of this product depending upon the non-Newtonian model, $\pi=e_{ij}e_{ij}$, e_{ij} is the $(i,j)^{th}$ constituents of distortion rate, which can be explicitly stated as

$$e_{ij}=-PI+\mu A_1 \qquad \ldots(3)$$

In which, P refers indeterminate pressure, I indicates the identity tensor, μ symbolize dynamic viscosity, A_1 depicts the Rivilin Erickson tensor of the first kind.

The Cauchy stress tensor regarding Williamson non-Newtonian fluid model is presented below[14]

$$\bar{\tau}_{ij}=\mu\left[\frac{\partial u}{\partial y}+\Gamma\left(\frac{\partial u}{\partial y}\right)^2\right] \qquad \ldots(4)$$

in which Γ represents the time constant, it is noteworthy that, at $\Gamma=0$, the first expression on the right side, refers to the Newtonian model. Consequently, the integrated stress tensor for Casson-Williamson fluid model is expressed as

$$\tau_{ij} = \mu\left[\left(1+\frac{1}{\beta}\right)\frac{\partial u}{\partial y} + \Gamma\left(\frac{\partial u}{\partial y}\right)^2\right] \quad \ldots (5)$$

in which, $\beta = \mu_\varepsilon \frac{\sqrt{2\pi_c}}{P_y}$ is the Casson fluid parameter.

The leading equations incorporating all above assumptions are developed as follows[27]

$$\frac{\partial u}{\partial x} + \frac{\partial v}{\partial y} = 0 \quad \ldots(6)$$

$$\frac{\partial u}{\partial t} + u\frac{\partial u}{\partial x} + v\frac{\partial u}{\partial y} = \frac{\partial U_\infty}{\partial t} + U_\infty \frac{\partial U_\infty}{\partial x} + \left[\nu\left(1+\frac{1}{\beta}\right) + 2\nu\Gamma\frac{\partial u}{\partial y}\right]\frac{\partial^2 u}{\partial y^2} - \frac{\sigma B_0^2}{\rho}\left(u - U_\infty\right) \pm g\left[\beta_T\left(T - T_\infty\right) + \beta_c\left(C - C_\infty\right)\right] \quad \ldots(7)$$

$$\frac{\partial T}{\partial t} + u\frac{\partial T}{\partial x} + v\frac{\partial T}{\partial y} = \frac{\kappa}{\rho C_p}\frac{\partial^2 T}{\partial y^2} - \frac{1}{\rho C_p}\frac{\partial q_r}{\partial y} + \tau\left[D_B\frac{\partial C}{\partial y}\frac{\partial T}{\partial y} + \frac{D_T}{T_\infty}\left(\frac{\partial T}{\partial y}\right)^2\right] + \frac{Q_0}{\rho C_p}\left(T - T_\infty\right) + \frac{\sigma B_0^2}{\rho C_p}\left(u - U_\infty\right)^2 + \frac{D_B K_T}{c_s C_p}\frac{\partial^2 C}{\partial y^2} + \frac{\mu}{\rho C_p}\left[\left(1+\frac{1}{\beta}\right)\left(\frac{\partial u}{\partial y}\right)^2 + \Gamma\left(\frac{\partial u}{\partial y}\right)^3\right] \quad \ldots(8)$$

$$\frac{\partial C}{\partial t} + u\frac{\partial C}{\partial x} + v\frac{\partial C}{\partial y} = D_B\left(\frac{\partial^2 C}{\partial y^2} + \frac{K_T}{T_m}\frac{\partial^2 T}{\partial y^2}\right) \quad \ldots(9)$$

contingent on deliberated geometry the boundary conditions are given below

$$u = U_s,\ v = -\frac{v_s}{\sqrt{1-\delta t}},\ T = T_s,\ C = C_s \quad at \quad y = 0$$
$$u \to U_\infty,\ T \to T_\infty,\ C \to C_\infty \quad as \quad y \to \infty \quad \ldots (10)$$

in which, u and v denote the constituents representing velocity in $x-$ and $y-$ directions respectively, ν is the kinematic viscosity, σ refers fluid electrical conductivity, ρ refers the density, g is the gravitational acceleration, β_T and β_C are solutal thermal and concentration expansion factors, κ is the thermal conductivity, C_p is the specific heat at constant pressure, q_r is the radiative thermal flux, τ is the heat capacity ratio, D_B and D_T refer Brownian and thermophoresis diffusion coefficients, Q_0 stands for the coefficient of thermal energy generation/absorption, K_T is the heat diffusion ratio, c_s is the mass susceptibility, T_m shows the fluid mean temperature, and v_s refers mass transport rate.

The ensuing similarity variables are utilized to tackle the above set of equations

$$\eta = \sqrt{\frac{c}{(1-\delta t)\nu}}\,y, \quad u = \frac{cx}{(1-\delta t)}f'(\eta),$$
$$v = -\sqrt{\frac{c\nu}{(1-\delta t)}}\,f(\eta), \quad \ldots(11)$$
$$T = T_\infty + (T_s - T_\infty)\theta(\eta),$$
$$C = C_\infty + (C_s - C_\infty)\Phi(\eta)$$

The above system of Eqs. (6)-(9) attains the following form after implementation of above transformation

$$\left[\left(1+\frac{1}{\beta}\right) + We\,f''\right]f''' + \left(f - \frac{A\eta}{2}\right)f'' - f'^2 - (A+M)f' \pm \lambda_T(\theta + R\Phi) + (A+M)r + r^2 = 0 \quad \ldots(12)$$

$$(1+Nr)\theta'' + \Pr\left(f - \frac{A\eta}{2}\right)\theta' + \Pr Nb\,\theta'\Phi' + \Pr Nt\,\theta'^2 + M\,Br\left(f' - r\right)^2 + Br\left(1+\frac{1}{\beta}\right)f''^2 + \frac{Br\,We}{2}f''^3 + \Pr Q\theta + \Pr Du\,\Phi'' = 0 \quad \ldots(13)$$

$$\Phi'' + Sc\left(f - \frac{A\eta}{2}\right)\Phi' + ScSr\,\theta'' = 0 \quad \ldots(14)$$

The improved extremities conditions

$$f' = 1,\ f = S,\ \theta = 1,\ \Phi = 1 \quad at \quad \eta = 0$$
$$f' \to r,\ \theta \to 0,\ \Phi \to 0 \quad as \quad \eta \to \infty \quad \ldots(15)$$

in which, prime $'$ refers the derivative of the function concerning η, $We = \frac{2}{\sqrt{\mathrm{Re}_x}}\Gamma\frac{U_s^2}{\nu}$ denotes the

local Weissenberg number, $\mathrm{Re}_x = \frac{U_s x}{\nu}$ is the local Reynolds number, $A = \left(\frac{\delta}{c}\right)$ is unsteadiness parameter, $M = \frac{\sigma B_0^2 \mathrm{Re}_x \nu}{\rho U_s^2}$ is magnetic field parameter, $\lambda_T = \frac{Gr_{x,T}}{\mathrm{Re}_x^2}$ is the thermal buoyancy parameter, $\lambda_C = \frac{Gr_{x,C}}{\mathrm{Re}_x^2}$ is the mass buoyancy parameter, $Gr_{x,T} = \frac{g\beta_T (T_s - T_\infty)x^3}{\nu^2}$, $Gr_{x,C} = \frac{g\beta_C (C_s - C_\infty)x^3}{\nu^2}$, $R = \frac{Gr_{x,C}}{Gr_{x,T}}$ is the buoyancy ratio parameter, $r = \frac{a}{c}$ represent stagnation point, $Nr = \frac{16\sigma^* T_\infty^3}{3k^*\kappa}$ relates radiation parameter[28], $\mathrm{Pr} = \frac{\nu}{\alpha}$ is the Prandtl number, $Nb = \frac{\tau D_B (C_s - C_\infty)}{\nu}$ shows the Brownian motion parameter, $Nt = \frac{\tau D_T (T_s - T_\infty)}{\nu T_\infty}$ is the thermophoresis parameter, $Br = \mathrm{Pr} Ec$ is the Brinkmann number, $Ec = \frac{U_s^2}{C_p (T_s - T_\infty)}$ is the Eckert number, $Q = \frac{Q_0 \mathrm{Re}_x \nu}{\rho C_p U_s^2}$ signifies heat generation $(Q > 0)$ or heat absorption $(Q < 0)$ parameter, $Du = \frac{D_B K_T (C_s - C_\infty)}{\nu (T_s - T_\infty) c_s C_p}$ stands for Dufour number, $Sc = \frac{\nu}{D_B}$ is the Schmidt number, $Sr = \frac{(T_s - T_\infty) D_B K_T}{\nu (C_s - C_\infty) T_m}$ stands for Soret number, and $S = \frac{v_s}{\sqrt{c\nu}}$ is the suction/injection parameter.

The dimensionless parameters of physical concern are local skin friction coefficient (C_f), Nusselt number (Nu_x), and Sherwood number (Sh_x), are expressed as follows

$$C_f = \frac{\tau_s}{\frac{1}{2}\rho U_s^2}, \quad Nu_x = \frac{x q_s}{\kappa (T_s - T_\infty)}, \quad Sh_x = \frac{x q_m}{D_B (C_s - C_\infty)} \qquad \ldots(16)$$

in which, $\tau_s = \mu \left[\left(1 + \frac{1}{\beta}\right) \frac{\partial u}{\partial y} + \Gamma \left(\frac{\partial u}{\partial y} \right)^2 \right]_{y=0}$ is the surface shear stress, $q_s = \left(-\kappa \frac{\partial T}{\partial y} + q_r \right)_{y=0}$ shows the heat gradient at surface, $q_m = \left(-D_B \frac{\partial C}{\partial y} \right)_{y=0}$ is the surface mass gradient.

Employing the similarity transformations of Eq. (11) in the above Eq. (16) the resultant expressions are obtained as

$$C_f \sqrt{\mathrm{Re}_x} = 2\left(1 + \frac{1}{\beta}\right) f''(0) + We\, f''^2(0) \qquad \ldots(17)$$

$$\frac{Nu_x}{\sqrt{\mathrm{Re}_x}} = -(1 + Nr)\theta'(0) \qquad \ldots(18)$$

$$\frac{Sh_x}{\sqrt{\mathrm{Re}_x}} = -\Phi'(0) \qquad \ldots(19)$$

3 Solution approach

The system of ordinary differential equations (ODEs) described in Eq. (12)-(14), along with the boundary conditions specified in Eq. (15), exhibits highly nonlinear behavior. The complexity of these nonlinearities presents a considerable obstacle to applying conventional numerical methods. Hence, a specialized built-in algorithm, BVP Midrich in Maple software, is employed to obtain a numerical solution for the system. The flow chart of this scheme is presented in Fig. 2.

To assess the accuracy of the results, the current outcomes are compared with the results by Mahmoud[29] and Yousef *et al.*[30]. Table 1 illustrates the validation of the computational data for surface shear stress across various estimates of the magnetic parameter (M).

4 Analysis of the results

This segment evaluates the impression of all relevant parameters on fluid velocity, thermal, and mass profile via graphical representation. Variations in shear stress, heat flux, and mass flux at the surface are inspected through numerical data displayed in the table. All other parameters while discussing one, are set to fixed as $\beta = 0.5, We = 1, A = 0.2, M = 1,$

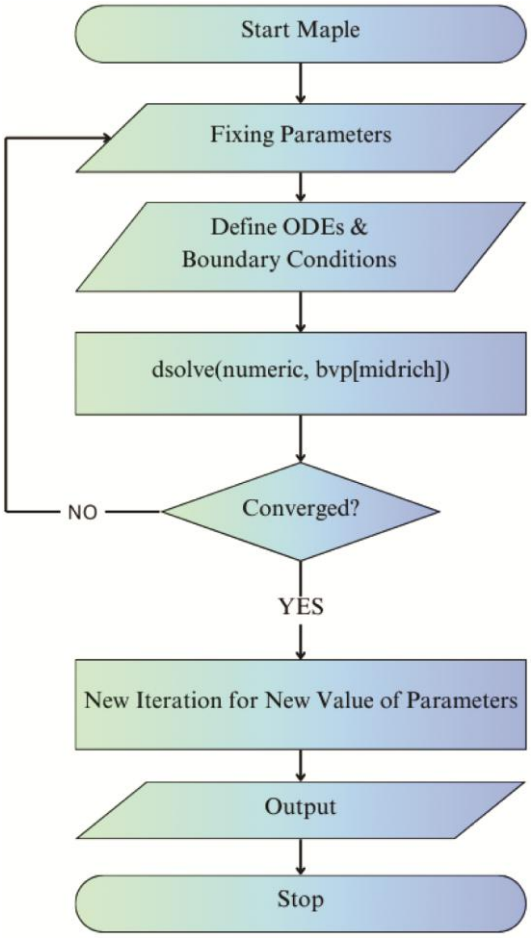

Fig. 2— Flow chart of BVP Midrich method

Table 1 — Comparison of $-f''(0)$ values with results of two previously published articles when $We = 0 = A = \lambda_T = R = r = S$ and $\beta \to \infty$.

M	Mahmoud[29]	Yousef *et al.*[30]	Present results
0	1.00140	1.00139983	1.0042581647
1	1.41424	1.41422875	1.4144154842
3	2.00000	2.00000000	2.0000019841
5	2.44950	2.44948791	2.4494897978

$\lambda_T = 1,\ R = 0.5,\ r = 1.0$ (Ref.[24]), $S = 0.5,\ Nr = 1,$ $\Pr = 2.0,\ Nb = 0.5,\ Nt = 0.2,\ Br = 1,\ Q = 0.5,$ $Du = 0.5,\ Sc = 2,\ Sr = 0.2.$

Table 2 reveals that in the buoyancy assisting flow domain, skin friction coefficient, and surface heat transfer rate possess similar trends for $\beta, We, A, \lambda_T, R, Nt, Br, Q, Du, Sr$ and dissimilar behavior for $M, r, S, Nr, Nb,$ and Sc. In the buoyancy opposing flow field, the skin friction coefficient retains the opposite response for all parameters as in the buoyancy assisting flow field, excluding We and r. The surface mass transfer rate enhances against We, A, M, Nr, Nb and diminishes for all remaining parameters in the buoyancy assisting flow field. Local Nusselt and Sherwood numbers both possess reversal trends except β, We, A, M, r in buoyancy opposing flow regions.

The variations in momentum and thermal profiles against the Casson parameter (β) are demonstrated in Figs. 3(a & b). In the buoyancy-supportive region, the fluid velocity gets higher adjacent to the sheet but decelerates away from the sheet for increasing values of β. On the contrary, velocity decelerates drastically nearby the sheet, and a converse trend follows at a distance for buoyancy opposing flow. This addresses the fact that developing fluid viscosity for augmentation in β appears with enhancement in yield stress, which, consequently, stands responsible for acquired changes in fluid momentum. Furthermore, it is ascertained that as $\beta \to \infty$ the nature of fluid turns as a Newtonian fluid, the velocity escalates immensely inside the layer of fluids near the vertical wall. The temperature profile shows slightly increasing and decreasing movement across the buoyancy supportive and resisting flow areas.

The characteristics of local Weissenberg number (We) on momentum and temperature distribution are discussed through Figs. 4(a & b). The variation in We controls both the fluid flow and the temperature. There is a minor reduction in the velocity field in the buoyancy-supporting zone and minor augmentation in the buoyancy-resisting zone for increasing values of We. Physically, the dimensionless parameter Weissenberg number is characterized as the proportion of relaxation time to the processing time. Elevating values of We enhance the relaxation time; this indicates that particles take more time to slow down from the perturbed system, reducing fluid momentum. The temperature profile shows significant variation for increasing values of We.

Figures 5 (a & b) deal with the consequences of magnetic parameter (M) on momentum and temperature profiles. The more significant impact of magnetic field force drives deceleration in fluid velocity in the buoyancy-supporting field, and the converse trait follows in the buoyancy-resisting field. It stems from the reason that the growing effect of

Table 2— Numerical data of $C_f\sqrt{\mathrm{Re}_x}$, $\theta'(0)$ and $\Phi'(0)$ in both buoyancy assisting and buoyancy opposing flow region, for various flow controlling parameters at $\mathrm{Pr} = 2$.

β	We	A	M	λ_T	R	r	S	Nr	Nb	Nt	Br	Q	Du	Sc	Sr	$C_f\sqrt{\mathrm{Re}_x}$		$\theta'(0)$		$-\Phi'(0)$	
																Buoyancy assisting	Buoyancy Opposing	Buoyancy assisting	Buoyancy opposing	Buoyancy assisting	Buoyancy opposing
0.5	1	0.2	1	1.0	0.5	1.0	0.5	1	0.5	0.2	1	0.5	0.5	2	0.2	1.6124921	-1.6823280	0.2660795	0.3344433	2.0169116	1.9775087
1.0																1.4857158	-1.5373454	0.2651042	0.3517691	2.0236271	1.9726271
1.5																1.4315037	-1.4658512	0.2646023	0.3605566	2.0267761	1.9696566
2.0																1.4013227	-1.4216558	0.2642994	0.3660179	2.0286116	1.9676082
∞																1.3514627	-1.3362879	0.2637610	0.3765134	2.0317866	1.9631426
0.5	2															1.6242085	-1.6664677	0.2660795	0.3355822	2.0169116	1.9771121
	3															1.6351713	-1.6485114	0.2660994	0.3368934	2.0164784	1.9766426
	4															1.6454886	-1.6275159	0.2661418	0.3384580	2.0157140	1.9760630
	5															1.6552453	-1.6013596	0.2661636	0.3404615	2.0153728	1.9752869
	1	0.4														1.6484440	-1.7337364	0.3081327	0.3932723	1.9713554	1.9305294
		0.6														1.6901567	-1.7982982	0.3571148	0.4678040	1.9255532	1.8845958
		0.8														1.7393754	1.8838290	0.4155036	0.5684548	1.8801651	1.8426299
		1.0														1.7986311	-2.0079246	0.4870961	0.7195907	1.8364382	1.8128671
		0.2	2													1.5201934	-1.5688949	0.2667470	0.3271228	2.0146683	1.9783829
			3													1.4436401	-1.4786411	0.2671926	0.3214361	2.0128156	1.9790551
			4													1.3786500	-1.4042658	0.2674998	0.3168612	2.0112519	1.9795964
			5													1.3224709	-1.3413887	0.2677164	0.3130829	2.0099090	1.9800467
			1	0.5												0.8110564	-0.8277073	0.2590560	0.2899575	2.0001617	1.9796867
				1.5												2.4096024	-2.5808274	0.2858031	0.4072484	2.0375075	1.9829060
				2.0												3.2067035	-3.5570520	0.3173647	0.5247265	2.0617995	2.0000029
				2.5												4.0075638	-4.7089637	0.3603291	0.7373532	2.0897538	2.0418090
				1.0	1.5											2.2494687	-2.3577397	0.2781734	0.3728561	2.0298241	1.9795732
					2.5											2.8831765	-3.0386473	0.2952383	0.4218475	2.0442886	1.9848262
					3.5											3.5133921	-3.7248317	0.3169692	0.4827819	2.0602068	1.9936843
					4.5											4.1399251	-4.4159254	0.3430816	0.5573215	2.0774874	2.0066583
					0.5	0.6										-0.8000996	-4.5533439	0.4558336	0.8375685	2.0059981	2.0447973
						0.8										0.3138192	-3.1517064	0.3181924	0.5100363	1.9963112	1.9883086
						1.2										3.0879383	-0.1130033	0.3043372	0.2761562	2.0690568	2.0031674
						1.4										4.7351289	1.5678650	0.4396362	0.3260213	2.1548759	2.0635050
						1.0	1.0									1.4384967	-1.4737289	0.3489041	0.3899038	2.8618862	2.8342517
							1.5									1.2848997	-1.3031593	0.4418752	0.4675657	3.7672530	3.7476953
							2.0									1.1526219	-1.1623309	0.5406908	0.5574744	4.7111813	4.6971465
							2.5									1.0397510	-1.0450288	0.6432394	0.6546330	5.6807093	5.6704730
							0.5	2								1.6699599	-1.7087740	0.0823802	0.0839481	1.9394880	1.8755187
								3								1.7143997	-1.7627393	0.0039297	0.0169935	1.9052984	1.8424644
								4								1.7468381	-1.7978838	-0.0401508	-0.0237989	1.8860753	1.8228817
								5								1.7703249	-1.8208520	-0.0692384	-0.0528228	1.8736799	1.8097277
								1	1.0							1.6588998	-1.7319948	0.3363233	0.3889134	2.0384882	1.9910732
									1.5							1.6960618	-1.7712590	0.3568234	0.3961169	2.0415984	1.9876082
									2.0							1.7254743	-1.8019088	0.3482361	0.3772183	2.0342578	1.9752231
									2.5							1.7486925	-1.8257687	0.3250076	0.3464307	2.0219929	1.9592565
									0.5	0.5						1.6793312	-1.7633511	0.3797553	0.4610937	2.0534521	2.0150202
										0.8						1.7551046	-1.8604356	0.5039439	0.6105905	2.0931210	2.0593829
										1.1						1.8430637	-1.9843724	0.6514112	0.8127460	2.1405782	2.1209712
										1.4						1.9494028	-2.1679941	0.8472066	1.1637063	2.2049726	2.2335231
											6					1.6441114	-1.7322897	0.4085010	0.5238556	2.0694170	2.0449021
											11					1.6802170	-1.7958858	0.5680431	0.7552453	2.1281287	2.1268888
											16					1.7222658	-1.8842655	0.5680431	1.0606802	2.1949688	2.2345357
											21					1.7725794	-2.0370308	0.9629358	1.5510089	2.2729781	2.4059979

(*contd.*)

Table 2 — Numerical data of $C_f\sqrt{\mathrm{Re}_x}$, $\theta'(0)$ and $\Phi'(0)$ in both buoyancy assisting and buoyancy opposing flow region, for various flow controlling parameters at $\mathrm{Pr}=2$. (*contd.*)

β	We	A	M	λ_T	R	r	S	Nr	Nb	Nt	Br	Q	Du	Sc	Sr	$C_f\sqrt{\mathrm{Re}_x}$		$\theta'(0)$		$-\Phi'(0)$	
																Buoyancy assisting	Buoyancy Opposing	Buoyancy assisting	Buoyancy opposing	Buoyancy assisting	Buoyancy opposing
10.1																1.4971720	-1.5373324	-0.0584844	-0.0294685	1.9031457	1.8564125
0.3																1.5501846	-1.6021410	0.0945332	0.1389159	1.9569726	1.9127582
0.7																1.6871692	-1.7860359	0.4620309	0.5705286	2.0848687	2.0547873
0.9																1.7788907	-1.9300289	0.6913777	0.8745065	2.1637542	2.1530174
0.5	0															1.3821208	-1.4226915	-0.4734397	-0.4294809	1.7536621	1.7164890
	1.0															1.6124921	-1.9908950	1.4094848	1.5335405	2.4342883	2.4046394
	1.5															1.8766596	-2.3735396	3.5121665	3.7871370	3.2238170	3.2410134
	2.0															2.1928490	-2.8826855	9.2463171	10.111088	5.4446074	5.6822121
	0.5	0.4														1.7838613	-1.8521425	-0.3676894	-0.2821115	0.6251874	0.5958105
		0.8														1.7235916	-1.8067921	-0.1869765	-0.1083451	0.9848400	0.9466821
		1.2														1.6711679	-1.7497249	-0.0316183	0.0422926	1.3262178	1.2858502
		1.6														1.6371873	-1.7107933	0.1169829	0.1876466	1.6670539	1.6266358
		2.0	0													1.6067162	-1.6775672	0.1712115	0.2332193	1.8033309	1.7476522
			0.4													1.6179756	-1.6867027	0.4136933	0.4901338	2.3499367	2.3322694
			0.6													1.6228746	-1.6903967	0.6709617	0.7572711	2.9339144	2.9453944
			0.8													1.6264218	-1.6925915	1.2012890	1.2913509	4.1620179	4.1992156

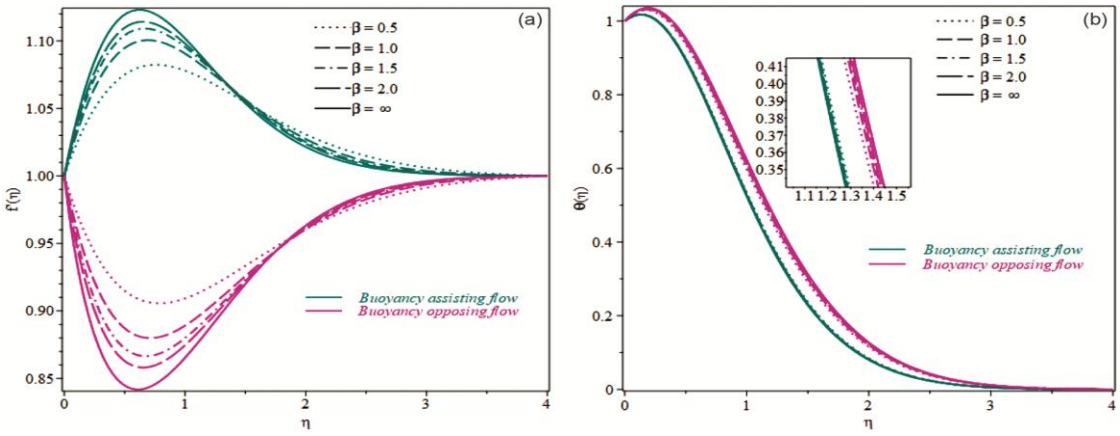

Fig. 3 — Variations in (a) $f'(\eta)$ (b) $\theta(\eta)$ against β

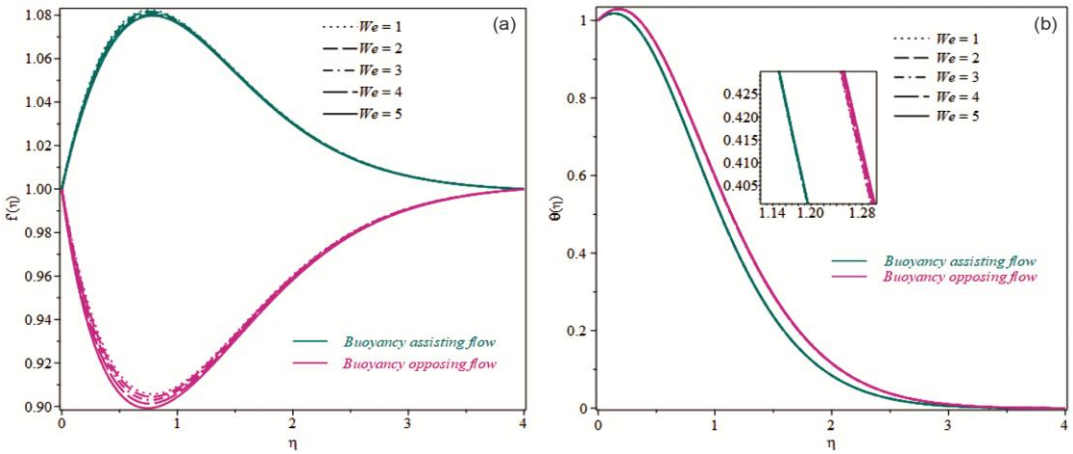

Fig. 4 — Variations in (a) $f'(\eta)$ (b) $\theta(\eta)$ against We

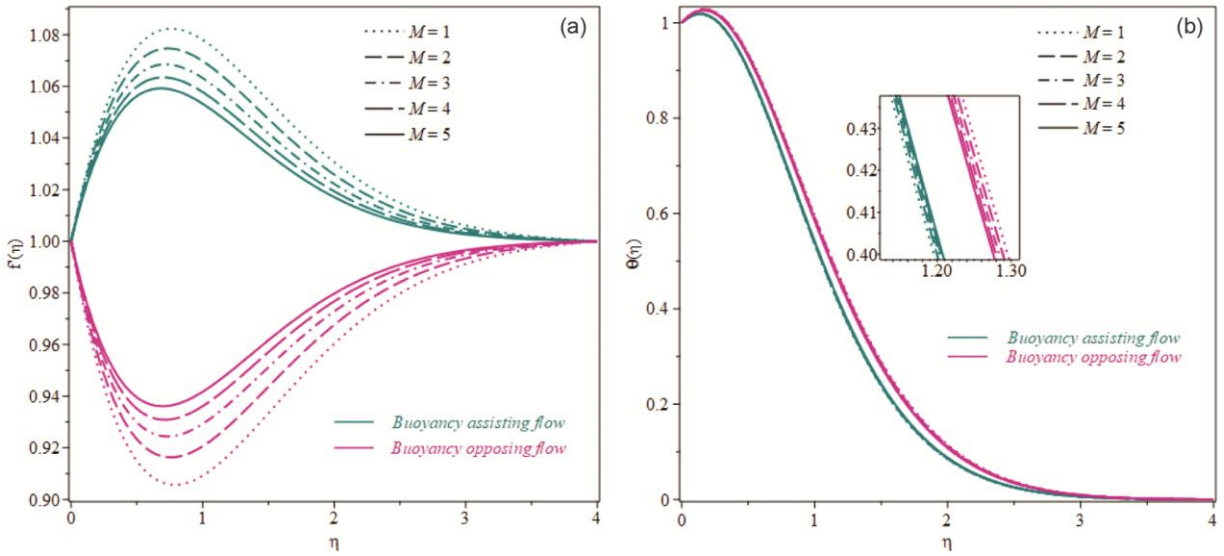

Fig. 5 — Variations in (a) $f'(\eta)$ (b) $\theta(\eta)$ against M

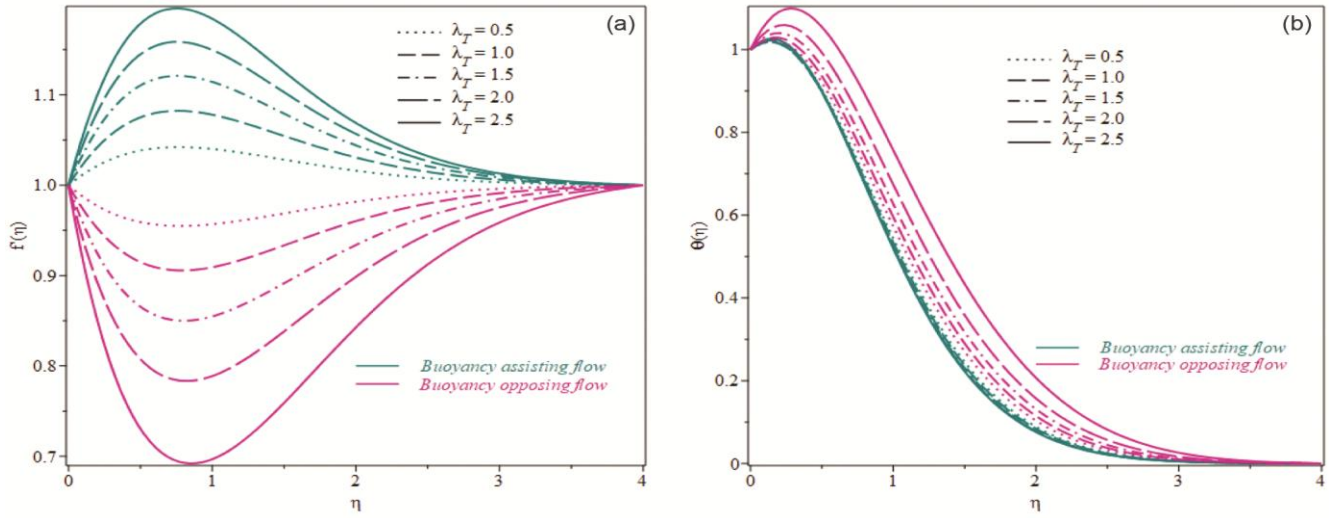

Fig. 6 — Variations in (a) $f'(\eta)$ (b) $\theta(\eta)$ against λ_T

magnetic field originates a resistive force stated as the Lorentz force; this force prompts resistance in the flow, due to which velocity decreases. This resistive force produces thermal energy in the fluid medium, resulting from which temperature shortly upsurges.

The deviations in fluid momentum and thermal profiles against thermal buoyancy parameter (λ_T) are demonstrated in Figs. 6(a & b). It is noted that fluid and momentum boundary layer thickness increases with values of λ_T in the buoyancy supporting flow area. In contrast, velocity reduces in the buoyancy opposing flow area. Physically, increasing values of λ_T raise the Grashof number values, and from the definition, it is apparent that the Grashof number is in inverse proportion with fluid kinematic viscosity. Therefore, inflation in the Grash of number enhances the fluid velocity in the buoyancy-assisting flow field. Fig. 6(b), shows that temperature gets higher in buoyancy opposing flow region, whereas it shows no significant impact in buoyancy assisting flow region.

Figures 7(a & b) explicate the variation in fluid temperature and concentration following the Brownian motion (Nb) parameter. This is interpreted with the figure that temperature is

increasing while concentration is diminishing function of Nb for both buoyancy-supporting and opposing fields. Brownian motion is the erratic locomotion of fluid particles. Such movement of fluid particles speeds up when the temperature is increased.

The consequences of thermophoresis occurrence (Nt) on the heat and mass distribution profile are portrayed in Figs. 8(a & b), respectively. Upgrading the constraint Nt results in a significant amplification in fluid temperature, with a slight diminution in mass profile near the sheet. Due to the increasing effect of thermophoresis, the fluid particles gain momentum and start having irregular strikes in the fluid medium. Due to this, a force is oriented towards lower temperatures. It raises the heat exchange rate and consequently the temperature in both buoyancy-supporting and resisting flow regions.

The influence of Brinkmann number (Br) on the thermal energy transfer performance of the fluid is illustrated in Fig. 9. From a physical perspective, the scenario can be explained by defining Br itself. The Brinkmann number measures the proportion of thermal energy generated by viscous dissipation to the thermal energy transmitted via molecular conduction. Greater estimates of Br cause more heat due to viscous dissipation, which improves the temperature and its boundary layer thickness.

Figure 10 is sketched to analyze the impact of heat generation/absorption parameter (Q) on the thermal profile. The figure shows growth in temperature distribution for a more significant influence of Q. The heat generation/absorption parameter is a dimensionless parameter that states the amount of heat generated or absorbed within the fluid. Here only the heat generation case is considered in the study,

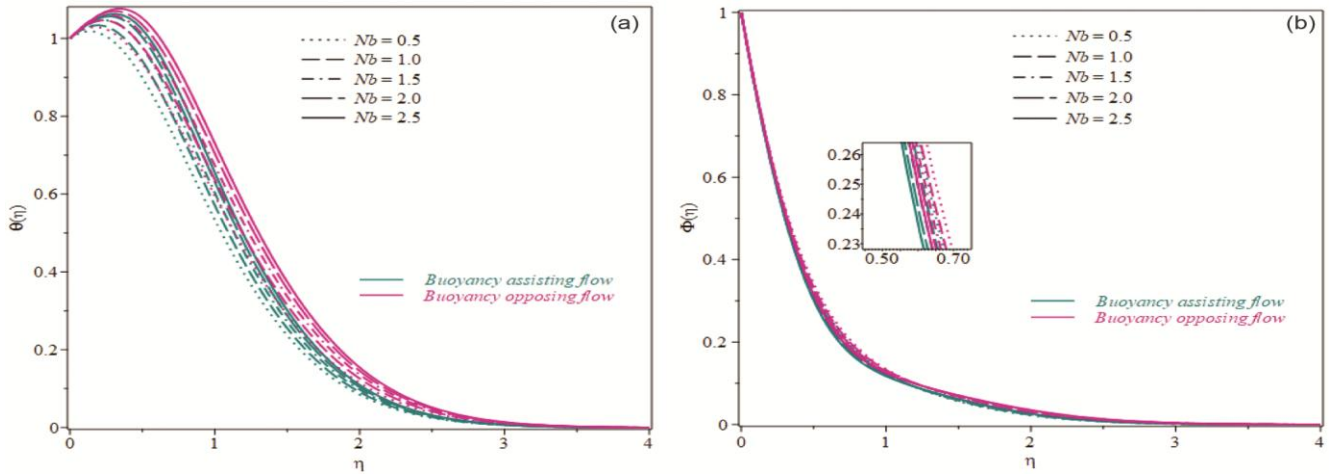

Fig. 7 — Variations in (a) $\theta(\eta)$ (b) $\Phi(\eta)$ against Nb

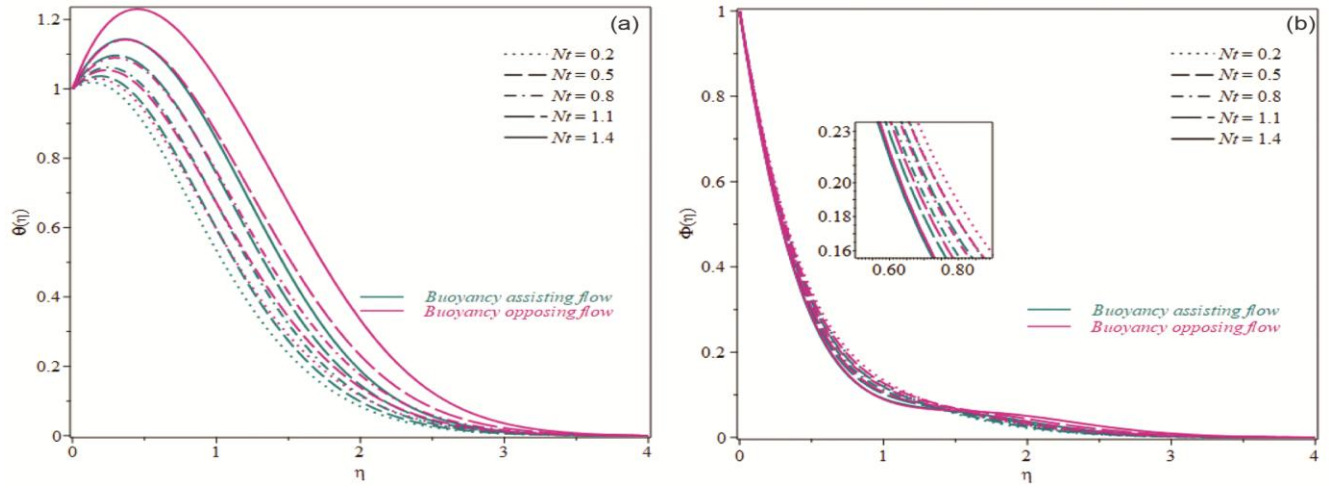

Fig. 8 — Variations in (a) $\theta(\eta)$ (b) $\Phi(\eta)$ against Nt

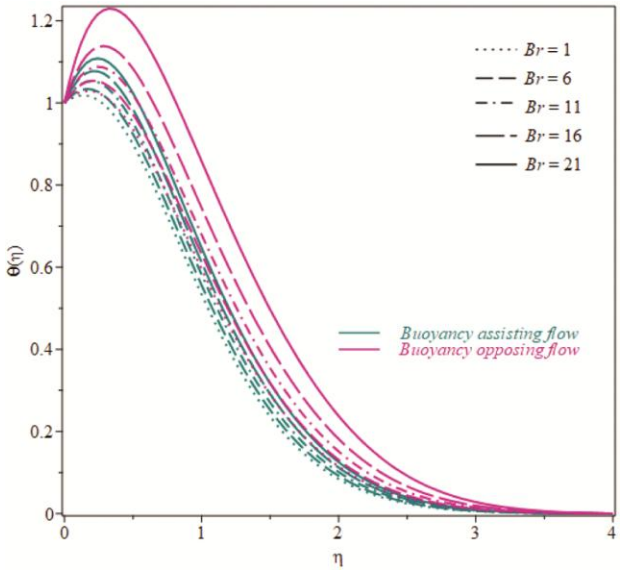

Fig. 9 — Variations in $\theta(\eta)$ against Br

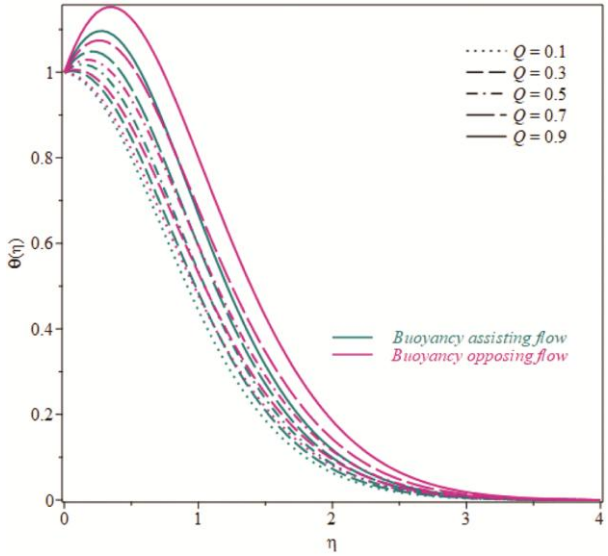

Fig. 10 — Variations in $\theta(\eta)$ against Q

and it is ascertained that heat generation supplies more heat in fluid, which boosts the thermal profile throughout the stream region. Moreover, the temperature is comparatively higher in the buoyancy opposing flow zone.

Figure 11 demonstrates the effect of Schmidt number (Sc) on the concentration profile. This is perceived from the figure that the concentration profile reduces throughout the flow region with higher values of Sc in both buoyancies supporting and contrasting flow regions. It is apparent from the definition that the Schmidt number possesses

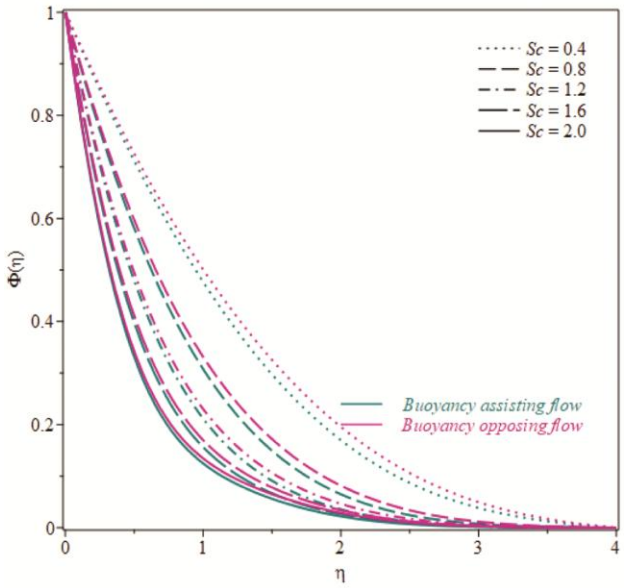

Fig. 11 — Variations in $\Phi(\eta)$ against Sc

inverse proportion with mass diffusivity. Therefore, growing values of Sc lead to a depreciation in mass diffusion, which lessens the concentration of fluid particles.

5 Conclusion

A numerical study concerning buoyancy assisting and opposing flow of Casson-Williamson fluid is performed by considering thermal radiation, Brownian motion, thermophoresis, and cross-diffusion effects. The mathematical model has functioned with the BVP Midrich scheme, and the resulting key points are summed up below

(i) The Casson fluid and thermal buoyancy parameters intensify the fluid velocity and buoyancy opposing thermal profile.

(ii) The velocity profile is decreasing while the thermal profile is an increasing function of the Weissenberg number and magnetic field parameter.

(iii) The thermal profile possesses a growing behavior against the rise in Brownian motion parameter, thermophoresis parameter, Brinkmann number, and heat generation/absorption parameter, which is quite the opposite of the concentration profile.

(iv) The skin friction coefficient and Nusselt number exhibit analogous qualitative demeanor for all parameters, excluding magnetic field, stagnation parameter, suction/injection, thermal radiation parameters, and Schmidt number in buoyancy assisting flow region.

(v) The surface heat and mass transfer rate both possess reversal responses except Casson fluid parameter, Weissenberg number, unsteadiness, magnetic and stagnation parameters in buoyancy opposing flow region. Also, the skin friction coefficient in the buoyancy-resisting flow region maintains a contradictory response as in buoyancy-supporting flow region for all parameters except the Weissenberg number and stagnation parameter.

References

1 Hanjalić K, *Annu Rev Fluid Mech*, 34 (2002) 321.
2 Well A J & Worster M G, *J Fluid Mech*, 609 (2008) 111.
3 Makinde O D, Khan W A & Khan Z H, *Int J Heat Mass Transf*, 62 (2013) 526.
4 Ahmad R, Mustafa M & Turkyilmazoglu M, *Int J Heat Mass Transf*, 111 (2017) 827.
5 Lund L A, Omar Z & Khan I, *Heliyon*, 5 (2019) e02432.
6 Iqbal Z, Khan M, Shoaib M, Matoog R T, Muhammad T & El-Zahar E R, *Waves Random Complex Media*, 5 (2022) 1.
7 Khan N A, Khan S & Riaz F, *Math Sci Lett*, 3 (2014) 199.
8 Nadeem S & Hussain S T, *Appl Nanosci*, 4 (2014) 1005.
9 Khan N A & Khan H, *Nonlinear Eng*, 3 (2014) 107.
10 Humane P P, Patil V S & Patil A B, *Proc Inst Mech Eng E J Process Mech Eng*, 235 (2021) 2008.
11 Kumaran G, Sandeep N & Ali M E, *Results Phys*, 7 (2017) 147.
12 Akolade M T & Tijani Y O, *Partial Differ Equ Appl Math*, 4 (2021) 100108.
13 Ogunseye H A, Salawu S O & Fatunmbi E O, *Partial Differ Equ Appl Math*, 4 (2021) 100148.
14 Humane P P, Patil V S, Patil A B, Shamshuddin M D & Rajput G R, *Proc Inst Mech Eng E*, 236 (2022) 1906.
15 Jangid S, Mehta R, Mehta T & Sushila, *Math Methods Appl Sci*, 46 (2023) 8243.
16 Hayat T, Shehzad S A & Alsaedi A, *Appl Math Mech*, 33 (2012) 1301.
17 Kumaran G & Sandeep N, *J Mol Liq*, 233 (2017) 262.
18 Mabood F, Yusuf T A & Sarris I E, *Spec Top Rev Porous Media*, 11 (2020) 595.
19 Venkata Ramudu A C, Anantha Kumar K, Sugunamma V & Sandeep N, *J Therm Anal Calorim*, 147 (2022) 2653.
20 Buongiorno J, *J Heat Transf*, 128 (2006) 240.
21 Anbuchezhian N, Srinivasan K, Chandrasekaran K & Kandasamy R, *Appl Math Mech*, 33 (2012) 765.
22 Mahanthesh B & Joseph T V, *J Nanofluids*, 8 (2019) 870.
23 Mittal A S & Patel H R, *Phys A Stat Mech Appl*, 537 (2020) 122710.
24 Sulochana C & Mahalaxmi B, *Heat Transf*, 51 (2022) 2761.
25 Chaudhary S & Chouhan K K, *Numer Heat Transf A Appl*, 84 (2023) 732.
26 Mukhopadhyay S, *Chin Phys B*, 22 (2013) 074701.
27 Sindhu S & Gireesha B J, *Int Commun Heat Mass Transf*, 135 (2022) 106062.
28 Chaudhary S & Kanika K M, *J Porous Media*, 23 (2020) 27.
29 Mahmoud M A, *Phys A Stat Mech Appl*, 375 (2007) 401.
30 Yousef N S, Megahed A M, Ghoneim N I, Elsafi M & Fares E, *Alex Eng J*, 61 (2022) 10161.